Measuring the Maximum Capacity and Thermal Resistances in Phase-Change Thermal Storage Devices

Allison Mahvi[1,*], Kedar Prashant Shete[2], Adewale Odukomaiya[1], Jason Woods[1,*]

[1]National Renewable Energy Laboratory, 15013 Denver West Pkwy, Golden CO 80401, USA
[2]University of Massachusetts Amherst, 160 Governors Drive, Amherst MA 01003, USA
*Corresponding Authors: Allison.Mahvi@nrel.gov, Jason.Woods@nrel.gov

Abstract

Thermal energy storage can increase the efficiency of the electric grid by adding flexibility to thermal systems. The value of thermal storage is a function of its energy and power density, which are driven by the capacity and thermal resistances in the storage device. Measuring these properties in-situ at the device level is an important step to understanding the performance and improving the design of thermal storage systems. In this paper, we present methods to measure the total capacity and thermal resistances in heat exchangers with integrated phase change materials. These methods are demonstrated on two thermal storage devices—a 570-kWh ice-based storage tank and a 0.35-kWh graphite-tetradecane composite device. The results show how thermal resistances evolve with the state of charge and discharge rate in these devices and quantify the impact of applied pressure on the contact resistance in composite phase change material heat exchangers. The proposed method allows for easy comparison between different systems and provides information on the thermal bottlenecks limiting performance. Ultimately, these measurements will allow designers to make robust, high-performance thermal storage devices for next-generation thermal systems.

Nomenclature

A	fit constant [K m^2 W^{-1}]
B	fit constant [K m^2 W^{-1}]
Cap	capacity [kJ or Wh]
c_p	specific heat capacity [kJ kg^{-1} K^{-1}]
C_{rate}	heat transfer rate normalized to the total capacity ($\dot{Q}/Cap$) [hr^{-1}]
D_t	outer tube diameter [m]
dt	inverse of the sampling frequency [s]
dx	width of nodes in x-direction in numerical model [m]
E_{th}	thermal energy [kJ]
H	height [m]
h	heat transfer coefficient [W m^{-2} K^{-1}]
k	effective thermal conductivity [W m^{-1} K^{-1}]
L	latent heat [kJ kg^{-1}]
l	length [m]
M	mass [kg]
$\dot{m}$	fluid mass flow rate [kg s^{-1}]
N	node number in x-direction in numerical model [-]
$\dot{Q}$	heat transfer rate [W]
q''	heat flux [W/m^2]
R	resistance [K W^{-1}]
R''	area specific resistance [K m^2 W^{-1}]
SOC	state of charge [%]
S_t	distance between centerlines of adjacent tubes [m]
T	temperature [°C]
th	thickness [m]
W	width [m]

Greek Symbols

Δ	differential
μ	heat flux ratio at heat exchanger inlet

Superscripts

*	adjusted
$''$	area specific

Subscripts

a	active nodes in the x direction in the numerical model
ch	fully charged state
contact	related to contact resistance
disch	fully discharged state
eff	effective
f	heat transfer fluid
front	phase front location
glide	temperature glide
HX	heat exchanger
in	inlet
l	liquid
LM	log-mean
m	mean
max	maximum
min	minimum
out	outlet
PCM	phase change material
s	solid
sub	subcool
super	superheat
surf	surface
t	transition
total	total
wall	fluid channel wall
x	x direction

Introduction

Thermal energy storage (TES) can improve the flexibility of thermal systems by decoupling the production of heating or cooling from its use. TES has been considered for a wide range of systems to improve thermal management of electronic equipment[1,2] and to provide storage for buildings[3,4] and the electric grid.[5,6] Although several classes of materials have been considered for thermal storage, phase change materials (PCMs) have been studied extensively because they can accept or dispatch heat at a nearly constant temperature.[7-11]

There has been a significant amount of past work on evaluating PCM material properties but little progress on developing standardized procedures to characterize TES components (e.g., TES heat exchangers). In contrast, the electrochemical battery community has developed testing procedures to determine the total capacity, rate capability, energy and power densities, internal resistances, relaxation characteristics, and lifetime of a cell.[12] Rate capability and Ragone plots (comparison of energy and power density) for TES components have recently been developed by mimicking these electrochemical tests for batteries.[13] There may be additional opportunities to leverage electrochemical research to determine key properties of thermal storage components.

As with electrochemical storage, one of the most important characteristics of a TES device is its energy density at a given power. Thermal Ragone plots provide a way to compare different TES devices,[13] but give less insight on how they can be redesigned to achieve a higher energy density. The key properties that impact energy density are the total capacity and thermal resistances between the heat source or sink and the transitioning PCM. The capacity per unit volume quantifies the maximum possible energy density of the device, and the resistances drive how closely the device approaches this theoretical maximum. Both properties are commonly measured for new electrochemical battery architectures and chemistries using standard characterization techniques. The maximum capacity is typically measured by slowly discharging a cell,[12] which minimizes voltage losses. Capacity is measured on the device level to capture non-linear electrochemical phenomena, account for the anode and cathode geometry and consider diffusion rates in the device.[14]

For TES, capacity is rarely measured at the device level but instead is measured at the material level with differential scanning calorimetry. This technique measures the amount of heat required to change the temperature of a material, which for PCMs can give the sensible and latent capacity in the temperature range of interest. Although it is a useful tool for TES, differential scanning calorimetry will not account for any inactive components needed for device operation (for example, fluid channels), and more importantly it does not allow for in-situ capacity tests to see how performance changes with cycling under real operating conditions.

The electrical resistance is also commonly measured in electrochemical batteries under different loading and environmental conditions to determine current bottlenecks, define its operational bounds, and track its state of health.[15] Electrical resistances are typically measured with hybrid pulse power characterization, which applies consecutive charge and discharge current pulses at different C-rates.[12] The voltage response from this experiment can be used to determine the ohmic and polarization resistances of the cell as a function of the state of charge. These resistances can be disaggregated from the total by looking at how the voltage response develops over time.[16] First, an instantaneous drop in voltage occurs when a current is applied. This voltage drop is the result of ohmic resistance, which is the sum of the electrical resistances in anode, cathode, and current collectors, the contact resistance between the active mass and current collectors, and the ionic resistance through the electrolyte.[17] After this initial drop, the voltage continues to decrease due to charge-transfer and polarization resistances that develop as the cell discharges.

In a fluid-coupled TES device, there are three primary thermal resistances: the convective resistance of the fluid, the contact resistance between the fluid channels and PCM, and the internal resistance through the PCM. Like electrochemical cells, these resistances develop on different time scales. The convective and contact resistances (described as surface resistances in this work) are always present in the device, whereas the internal resistance develops as the device charges or discharges. Disaggregating these resistances can give useful insights into the limiting resistances, which can help designers develop high-performance TES systems. Additionally, measuring changes to the total resistance over time can quantify any degradation in the device's performance.

Resistances are rarely measured in TES devices, and the relative contributions of the surface and internal resistances are not usually determined. The total resistance is typically reported as the ratio of the driving temperature difference and the average heat transfer rate.[18] One study reported the measured resistances in a TES device coupled to a non-isothermal fluid stream, but the method to calculate these resistances was not described.[19] Past work has also measured the internal resistance through the PCM separately, but this was done by measuring the phase front location with embedded thermocouples at different distances from the fluid channel.[20] Although this is useful information, these types of measurements are often difficult or impossible to collect in packaged systems.

In this paper, we describe experimental methods that can be used to measure the capacity and resistances in TES devices, in contrast to the common techniques focused on just the TES material. The experimental protocols, assumptions, and limitations of the approaches are described in detail. We also demonstrate the methods on two TES devices—a 570-kWh ice-based component and a 0.35-kWh tetradecane composite device. These methods provide a pathway toward standardized TES characterization and will help designers improve the performance of these systems.

Methods

This section describes procedures for measuring the capacity and resistances in fluid-coupled TES devices. The methods presented here are designed to be in-situ measurements of TES as it is deployed, rather than inferring the device performance from PCM material properties alone.

Measuring Total Capacity. The first step in evaluating the performance of a thermal storage unit is to determine its total capacity. The total capacity (*Cap*) of a PCM-based device typically includes its latent heat (L) along with the capacity associated with additional subcooling and superheating above and below the transition temperature ($c_p \Delta T$), as shown in Equation 1.

$$Cap = M_{PCM}\left(c_{p,s}\Delta T_{sub} + L + c_{p,l}\Delta T_{super}\right) \quad (1)$$

The fully charged state is defined when all the active storage material is at T_{ch} ($T_{t,min} - \Delta T_{sub}$ for cold storage, where $T_{t,min}$ is the minimum phase change temperature of a PCM considering any temperature glide), and the fully discharged state is defined when all the material is at T_{disch} ($T_{t,max} + \Delta T_{super}$ for cold storage where $T_{t,max}$ is the maximum phase change temperature). One method to experimentally measure capacity is to determine the amount of heat that must be added or removed from a device to reach these isothermal charged and discharged states.

Figure 1 outlines a method to measure the capacity of a TES device when heat is added or removed using a heat transfer fluid. First, the storage device should be well insulated from the environment and connected to a flow loop that can supply fluid at a specified temperature and flow rate (see Figure 5 for an example). The experiment begins with a fully discharged TES device by setting the fluid inlet temperature to T_{disch}. Fluid should be supplied at this temperature until the outlet temperature changes by less than 0.02 °C over

a 15-minute period (dT/dt < 0.08 °C/h). We chose to maintain this state for 15 minutes to confirm an isothermal state and to accurately compute the average rate of change. These isothermal regions were not included when calculating the total capacity measurement, although including them has little impact on the measurement (< 1 Wh or 0.3% in this case) because the heat transfer rates are very low.

Once the isothermal condition is reached, we assume that all the storage material is at T_{disch}. This assumption can be verified either with an internal probe that measures the PCM temperature, or with a temperature sensor placed on the external surface of the device. After reaching the isothermal discharged state, the fluid inlet temperature should be set to T_{ch} until the outlet temperature changes by less than 0.02 °C over a 15-minute period. This same procedure can be run in reverse (going from the charged state to the discharged state) to verify the measurement.

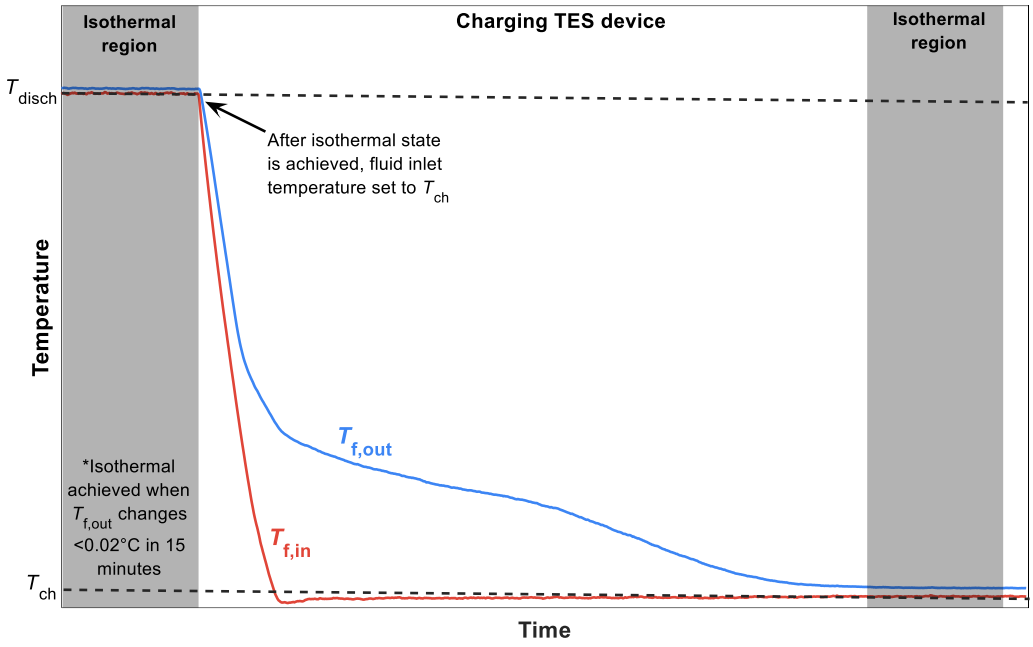

Figure 1: Capacity measurement method by charging TES device. The discharging capacity test is conducted by performing the sequence in reverse order.

The temperature difference across the fluid stream is often not exactly zero in the isothermal regions, which is likely the result of measurement uncertainty or continual heat losses or gains to/from the ambient. We adjusted the fluid outlet temperature to remove this offset. The measurement was adjusted by removing the average temperature difference between the outlet and inlet fluid streams during the isothermal periods (Equation 2).

$$T^*_{f,out} = T_{f,out} - \frac{\left(\bar{T}_{f,out} - \bar{T}_{f,in}\right)_{disch} + \left(\bar{T}_{f,out} - \bar{T}_{f,in}\right)_{ch}}{2} \quad (2)$$

Finally, the total amount of thermal energy that is added or removed from the device can then be calculated with the energy balance shown in Equation 3, where $\dot{m}_f$ is the fluid mass flow rate, $c_{p,f}$ is the fluid specific heat, and dt is the inverse of the sampling frequency. The sum of the thermal energy added or removed during each time step gives the total device capacity.

$$E_{th} = \int_0^t \dot{m}_f \, c_{p,f} \left| T^*_{f,out} - T_{f,in} \right| dt \tag{3}$$

Measuring Thermal Resistance. The thermal resistance in a TES device will initially be set by the surface resistances between the fluid and PCM and will increase over time as the phase front moves away from the tube wall. The total resistance can be evaluated with knowledge of the fluid heat transfer coefficient, contact resistance, and solid-liquid interface position, but these values are difficult to measure in-situ. In this section, we present a measurement method that can be experimentally executed on full TES heat exchangers and compare the resistances to the expected values based on the phase front location.

We used a validated transient finite difference numerical model[13] to compare the resistances calculated with these two approaches. The model simulates a device where heat is added or removed by a propylene-glycol water stream that passes through a high aspect ratio rectangular channel (0.25-m wide and 3-mm tall). The fluid channel is sandwiched between two form-stable composite PCM slabs containing tetradecane in a high-thermal-conductivity graphite matrix. The baseline phase change composite properties used in the model are a transition temperature of 4.6 °C, a temperature glide of 0.5 °C, a thermal conductivity of 10 W m^{-1} K^{-1} perpendicular to the fluid channel, and a latent heat of 168 kJ kg^{-1}.[13] The distance between adjacent tubes (the PCM slab thickness) was set to 7 cm. Heat was added to the device at a constant power, which was achieved by maintaining a constant flow rate and temperature difference between the fluid inlet and outlet streams (initially set to 4 °C). The model simulates the thermal performance of the device by discretizing the PCM composite into 800 subvolumes, and the fluid stream into 40 subvolumes in the axial direction. The heat transfer through the composite is calculated with a discretized version of Fourier's law, accounting for directional differences in thermal conductivity. The model determines the enthalpy change in each node with time and then calculates the enthalpy and temperature of each node with numerical integration using the explicit Euler approach. A more detailed description of the model and validation experiments are presented in Woods et al.[13]

This detailed numerical model can estimate the total resistance by summing the contributions of the fluid convective resistance ($1/h_f$), the tube wall conductive resistance (th_{wall}/k_{wall}), the contact resistance between the tube wall and the PCM composite ($R''_{contact}$), and the conductive resistance through the liquid PCM (L_{front}/k_{PCM}), as shown in Equation 4.

$$R_{total} = \frac{1}{2}\left[W_{HX} dx \sum_{i=N_a}^{N_x} \frac{1}{\frac{1}{h_{f,i}} + \frac{th_{wall}}{k_{wall}} + R''_{contact} + \frac{l_{front,i}}{k_{PCM}}} \right]^{-1} \tag{4}$$

Equation 4 only considers the "active" nodes of the device (denoted as N_a), defined as all x-locations where the PCM has not fully melted between the channel wall and the symmetry boundary condition. Once regions of the device fully melt, the PCM will start superheating and will not be bound by the transition temperature. Once this occurs, Equation 4 assumes that the total heat transfer rate into that region is negligible and the resistance to heat flow between the fluid and phase front is defined using the projected area of the phase front onto the tube wall (between N_a and N_x). This assumption is an estimate of the actual heat flows in the device,[13] and will result in some error.

Although this approach can be used to measure thermal resistance with a numerical model, it is difficult to evaluate experimentally. Generally, the distance between the phase front and channel surface cannot be

directly measured, and many carefully placed sensors are needed to accurately measure the surface resistance.

A second approach avoids the need for these measurements by estimating the resistance based on the fluid inlet and outlet temperatures during a constant power discharge. A constant power discharge experiment sets the fluid flow rate and control the inlet fluid temperature to maintain a constant temperature difference between the inlet and outlet streams ($\dot{Q}_f = constant = \dot{m}c_p\Delta T_f$). The total thermal resistance can then be calculated using the log-mean temperature difference, which is often used to evaluate the heat transfer rate between two fluid streams in a heat exchanger. In this case, the log-mean temperature difference is defined between the fluid and the phase front, which is at the maximum transition temperature (or simply the transition temperature if the phase transformation has no glide). The same approach can be used when measuring thermal resistances while charging a cold storage device or discharging a hot storage device (freezing the PCM). In this case, the phase front will be at the minimum transition temperature. The resistance is calculated with this temperature difference and the total heat transfer rate leaving the fluid stream, as shown in Equation 5. The total resistance can also be represented as an area-specific resistance, which allows for easier comparison between different TES heat exchanger sizes. In this work, all area-specific resistances are the product of the total resistance and the outer tube surface area in contact with the PCM or PCM composite.

$$R_{total} = \frac{1}{\dot{Q}_f}\left[\frac{\left(T_{f,in} - T_{f,out}\right)}{\ln\left(\frac{T_{f,in} - T_{t,max}}{T_{f,out} - T_{t,max}}\right)}\right] \tag{5}$$

Figure 2 shows the total thermal resistances calculated with Equations 4 and 5 for different C-rates and temperature glides. The log-mean temperature difference method is inaccurate if no phase front is present (near the beginning of the experiment before the PCM starts to transition phase) or when the PCM in a region of the device is fully melted or fully solidified. These regions are greyed out in Figure 2. The invalid regions can be identified with temperature measurements at the tube surface and adiabatic boundary, or with approximate approaches if internal thermocouples cannot be easily added. More information about identifying the boundaries of the grey regions is included in the supplemental section S1. When resistances are measured while cooling the PCM, supercooling can lengthen the invalid region because it delays the development of a phase front. This case is also discussed in the supplemental information.

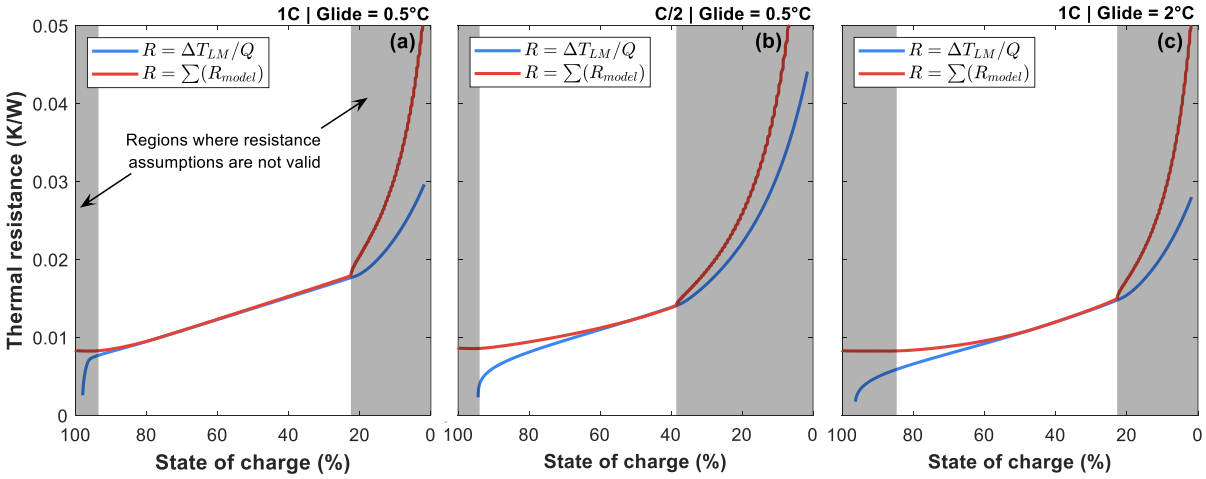

Figure 2: The total thermal resistance in the TES device measured using the location of the phase front and log-mean temperature difference method at (a) 1C and (b) C/2 when the material has a 0.5 °C temperature glide, and (c) at 1C when the material has a 2 °C temperature glide. The average transition temperature was lowered in (c) to have the same maximum transition temperature as (a) and (b).

The accuracy of the log-mean temperature difference approach depends on the PCM material properties and how fast the device discharges. For cold storage, Equation 5 assumes that heat passes from the heat transfer fluid to a thermal sink at the maximum phase change temperature. This assumption is valid if a solid-liquid interface is present across the entire length of the heat exchanger. At high states of charge, only a portion of the tube surface will be in contact with liquid PCM, causing the average heat sink temperature to be below the maximum phase change temperature (Figure 3a). When the baseline material is discharged at 1C, the log-mean temperature difference approach yields similar thermal resistances to those directly calculated with information about the phase front location (Equation 4) because the phase front grows more uniformly across the tube surface (Figure 3b). Liquid covers the entire tube after 75.4% state of charge, but the methods agree within 5% below 93% state of charge.

As the power decreases, the liquid layer develops unevenly (Figure 3c), and as the temperature glide increases, it takes longer for the liquid layer to develop because heat can be transported away from the tube surface more easily (Figure 3d). These both lead to deviations in the assumed heat sink temperature (Figure 3a), which result in errors in the thermal resistance calculated with the log-mean temperature difference approach (Figure 2b-c).

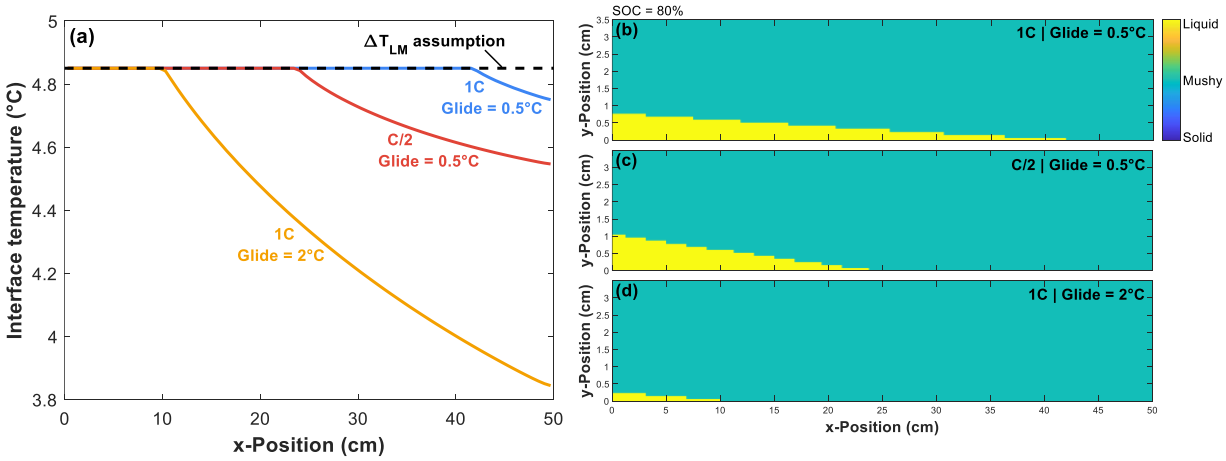

Figure 3: The log-mean temperature difference method assumes that the thermal sink is at the maximum phase change temperature, but at high states of charge a liquid layer has not formed across the entire tube and the thermal sink temperature near the outlet is lower than this assumption. The magnitude of the difference depends both on the material properties and operating conditions. The difference between the log-mean temperature difference assumption and the actual interface temperature (defined as the temperature at the surface of the tube when there is no liquid layer) at 80% state of charge is shown in (a), and (b-d) show the location of the phase front for different material properties and operating conditions.

It is important that the log-mean temperature difference approach is only applied when a liquid layer is present over most of the channel surface. Equations 6 and 7 show a rule of thumb to set the minimum C-rate for these resistance experiments. The equation assumes that the liquid layer varies linearly with x and extends the full length of the heat exchanger when the liquid fraction reaches 15%. This percentage was chosen because it results in good agreement between the two resistance calculations (Equations 4 and 5) below about 90% state of charge (Figure 2a). The main unknown parameter is μ, which is defined as the

ratio of the heat flux at the heat exchanger inlet to the average heat flux. This ratio is a function of the temperature glide and was found using the finite difference model described above. μ was set to 1.8, 1.3, and 1.2 for temperature glides of 0, 0.5, and 1 °C , respectively. In general, the higher the temperature glide, the lower the state of charge will be before 15% of the device is liquid. To reduce errors at high states of charge, the liquid fraction can be lowered, which will change μ and increase the minimum C-rate. The derivation for Equation 6 is shown in the supplemental section S2.

$$C_{rate,min} = \frac{2W_{HX}l_{HX}\Delta T_f}{\mu * Cap\left(R_{surf} + \frac{th_{in}}{k_{PCM}}\right)}\left[1 - \left(\frac{l_{HX}R_{surf}}{l_{HX}\left(R_{surf} + \frac{th_{in}}{k_{PCM}}\right)}\right)^{\frac{2W_{HX}l_{HX}k_{PCM}}{\dot{m}_f c_{p,f} th_{in}}}\right]^{-1} \quad (6)$$

$$\dot{m}_f = C_{rate,min}\frac{Cap}{c_{p,f}\Delta T_f} \quad (7)$$

Along with the total thermal resistance, the method described above can be used to disaggregate the internal resistance through the liquid layer from the surface resistance (convective, wall, and contact). For a constant power discharge, the PCM resistance is initially zero and increases linearly with state of charge until a portion of the device contains fully melted PCM (assuming the liquid PCM resistance is purely conductive). The log-mean temperature difference approach can directly measure this resistance if a uniform liquid layer appears instantaneously across the entire tube surface. In this case, the surface resistance will correspond to the value when the resistance first suddenly changes slope. Unfortunately, this condition almost never occurs. Instead, the resistance can be estimated by extrapolating the linear portion of the resistance curve to the state of charge where a liquid layer is expected to start forming. If thermocouples are placed on the surface of the fluid channels near the inlet port, the appropriate state of charge can be estimated when this surface temperature rises above the maximum transition temperature of the PCM (see supplemental section S2). If this measurement is not available, the surface resistance can be approximated by extrapolating to the saturated solid state of charge:

$$SOC_{sat,s} = 100\left(1 - \frac{M_{PCM}c_{p,s}\Delta T_{sub}}{Cap}\right) \quad (8)$$

Figure 4 shows the estimated surface resistances when the area-specific contact resistance in the model is set at 6, 16, and 26 K m^2 W^{-1}. In this case, the state of charge where liquid starts to form is evaluated using the tube surface temperatures (average state of charge = 92.4%). This approach underestimates the surface resistances by 6.6%, 2.8%, and 1.5%, respectively. If Equation 8 is instead used to estimate when liquid starts to form, the errors are slightly higher at 11.8%, 7.5%, and 5.7%, respectively.

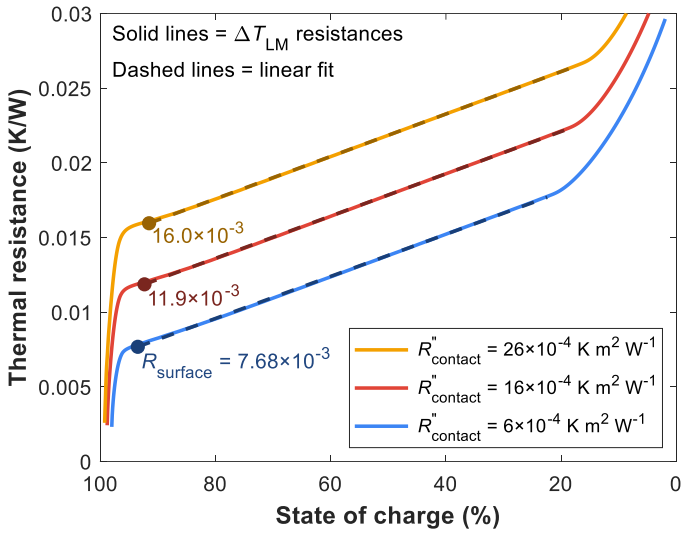

Figure 4: The total resistances calculated with the log-mean temperature difference approach and the estimated surface resistances, based on output from the finite difference numerical model.

Experiments

We demonstrated the proposed characterization methods using two different thermal storage devices. The first was a microchannel PCM composite heat exchanger similar to the device described above. Heat is passed in and out of the storage material by a propylene glycol – water mixture that flows through an array of microchannels (Figure 5a). This array contains 135 individual microchannel ports with hydraulic diameters of 1.3 mm. The flow is split evenly into the microchannel ports by a common manifold. Rectangular slabs (41.9 cm × 25.9 cm × 3.6 cm) of a graphite/tetradecane PCM composite are placed above and below the microchannel array. We found that tetradecane leaked out of the graphite material when cycled, so each slab was encapsulated in a heat-sealed Mylar bag. The bag increases the surface resistance but avoids the loss of capacity over time.

The inlet temperature and flow rate of the glycol mixture is controlled using the facility shown in Figure 5b. The test section is charged by supplying glycol below the PCM transition temperature to the fluid inlet. While charging, the heater is off and the temperature is controlled by a constant temperature circulating bath (Fisher Scientific 6200 R35). The device can be discharged by supplying glycol at a constant inlet temperature (capacity experiment) or by maintaining a constant heat transfer rate into the PCM composite(resistance experiment). The circulating bath is used to supply a constant inlet temperature, and a 1-kW external heater (Watlow FLUENT) is used to achieve a constant heat transfer rate by maintaining a constant temperature difference between the fluid inlet and outlet. For all constant power tests, the fluid temperature difference was set at 4.5 °C and the flow rate was varied to achieve the desired heat transfer rate. The flow rate was controlled using a DC power supply connected to a variable speed diaphragm pump. Pressure was applied to the top of the test section with a screw clamp to improve the thermal contact between the channel walls and the PCM composite. The applied force was measured with a load cell (Omega LC304-5K).

The heat transfer rate into and out of the fluid stream was measured using the fluid inlet and outlet temperature and the flow rate. The fluid temperatures were measured with three T-type thermocouples in each location. The thermocouples were calibrated using a constant-temperature bath and a NIST-traceable temperature probe. The average fluid temperature at each location was measured within ±0.1 °C. The flow rate was measured with a turbine flow meter (Omega FTB602B) with an accuracy of ±1% of the reading. T-type surface thermocouples were also placed on the external surface of the encapsulating Mylar bag on

the channel and insulation side of the test section, as shown in Figure 5b. The surface probes were placed 3 cm from the fluid inlet, 3 cm from the fluid outlet, and in the center of the device.

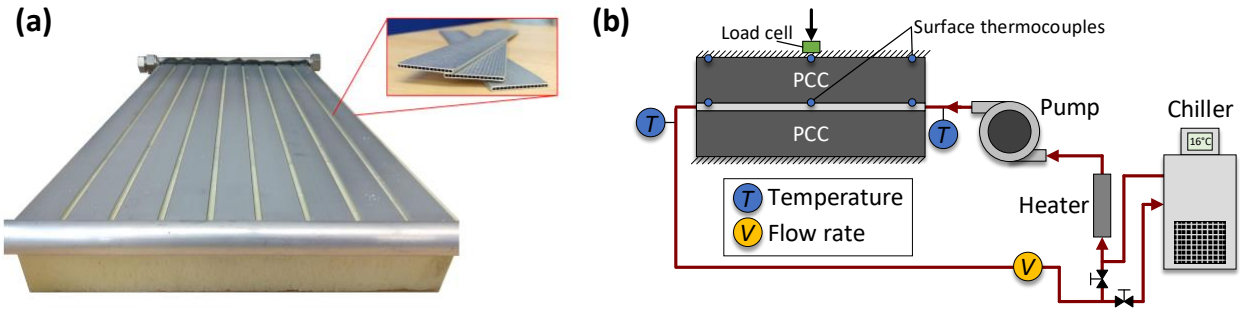

Figure 5: (a) The microchannel heat exchanger that allows propylene glycol-water to pass in and out of the test section to charge or discharge the PCM, and (b) a schematic of the experimental facility where the instruments marked with *T* and *V* are thermocouples and a volumetric flow meter, respectively.

We also measured the thermal resistances in an ice-based thermal storage device (CALMAC 1190). The device is used to store cooling for buildings by freezing 6,265 L of water. The water is contained in a large tank with a plastic heat exchanger coil. The coil allows propylene glycol – water to pass through the tank to add or remove heat. This storage device has a total capacity of 570 kWh.

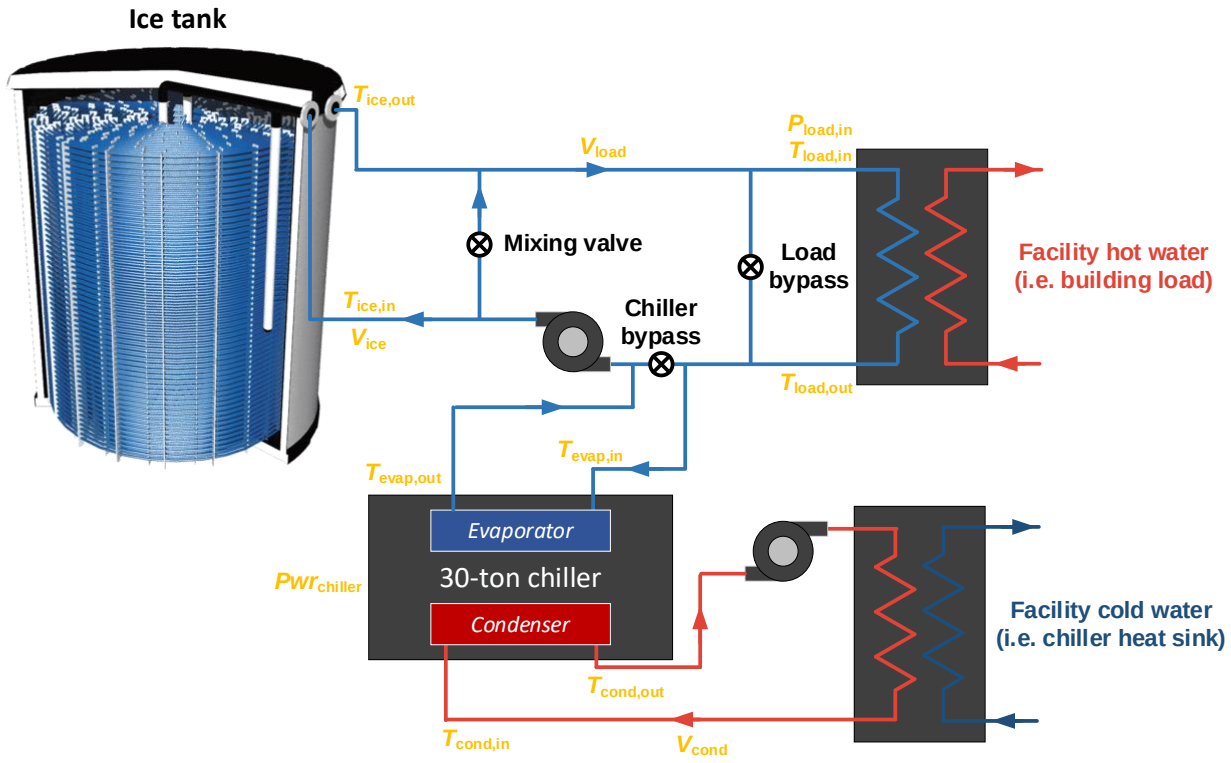

Figure 6: A schematic of the experimental facility used to measure the internal thermal resistances in a 570-kWh ice-based thermal storage system. Some of the main temperature (labeled T), flow rate (labeled V), pressure (labeled P), and power (labeled Pwr) measurements are shown in yellow. The ice tank image is used with permission from Trane Technologies.

The ice tank was connected to the facility shown in Figure 6 and charged using a 30-ton variable speed chiller (supplied by Trane). In these experiments, the thermal resistance between the glycol and the solid ice was measured while discharging the TES tank at a constant power. During discharge, the load bypass valve was closed, the chiller bypass valve was open, and the mixing valve was closed, forcing all the flow to pass through the ice tank and the heat exchanger coupled to the facility hot water system. The flow rate of the facility hot water stream was controlled using a control valve (Belimo P2200S series) to maintain a constant temperature difference between the ice tank inlet and outlet of 8.3 °C. The flow rate of the main flow loop was set to meet the target heat transfer rate using a variable speed pump (Price Pump Co, Model CD150). T-type thermocouples were used to measure fluid temperatures, and a turbine flow meter (Hoffer HO series) was used to measure the glycol flow rate through the ice tank. There were no temperature sensors inside the ice tank in this experiment. The tank was discharged over approximately 4-, 6- and 8-hour periods (C/4 to C/8), corresponding to heat transfer rates of 129, 94, and 72 kW.

Results

Total Capacity. The total capacity of the ice-based thermal storage device was given by the manufacturer, but the capacity of the PCM composite-based device was unknown. The fully charged state of the composite device was set at 0 °C, and a fully discharged state was set at 10 °C. The capacities measured by both charging and discharging the component are shown in Figure 7. The PCM composite was considered isothermal when the fluid outlet temperature changed by less than 0.02 °C over a 15-minute period (as described in the methods section). This assumption was validated in these experiments using thermocouples placed at the surface between the PCM composite and the insulation to confirm that the temperatures were below the transition temperature, indicating that the device was fully charged (see supplemental section S1). The temperature difference between the heat transfer fluid inlet and outlet was 0.13 °C (heat gain of 13±14 W) when held in the isothermal charged state. When the device was held in the isothermal discharged state, the temperature difference between the fluid inlet and outlet was approximately 0.01 °C, equating to a heat gain from the ambient of 1±14 W. To adjust for these interactions with the ambient, the fluid outlet temperature was adjusted by 0.07 °C according to Equation 2.

The measured capacities found by charging and discharging the device were similar, at 353±74 Wh and 368±63 Wh, respectively. We validated these measurements using a differential scanning calorimeter (TA Instruments Discovery DSC 2500) at a scanning rate of 1°C/min, which measured a latent heat of 161 kJ/kg. Using mass-averaged specific heats in the solid and liquid phase,[13] the expected device capacity between 0 and 10°C is 333 Wh, which is within the experimental uncertainty of the values calculated with this device-level measurement.

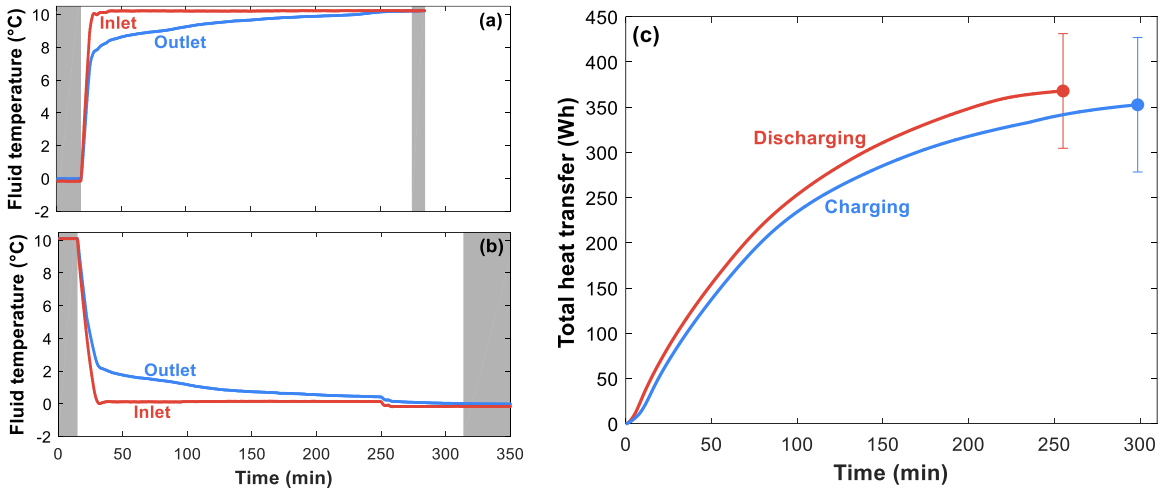

Figure 7: The measured fluid inlet and outlet temperatures while (a) charging and (b) discharging the device between defined charge and discharge states. The grey regions on the temperature plot mark isothermal periods of the test. The total heat transfer rate between these grey regions is shown in (c) where the circle indicates the total capacity. The uncertainty was calculated using the method described in supplemental section S5.

Resistances. The total thermal resistance in the PCM composite-based device was measured while supplying constant heat transfer rates between 350 and 700 W (C-rates between about 1 and 2). The maximum transition temperature used in the log-mean temperature difference equation was 6±0.5°C. This value is higher than the literature properties used in the model but was selected based on in-house temperature history experiments of the tetradecane used in the composite material (see supplemental section S4). The resistance results are shown in Figure 8a. The thermal resistance increases with state of charge but is not a strong function of the C-rate. The resistances are similar for different power rates because the graphite restricts the movement of tetradecane, resulting in conduction-dominated heat transfer. The fraction of liquid, and therefore the average liquid layer thickness, will depend primarily on the state of charge. Although the resistance will be somewhat impacted by the slope of the liquid layer, it does not have a large effect on the total resistance in this range of C-rates.

In contrast, resistance is a function of the heat transfer rate in the ice-based thermal storage device below about 50% state of charge (Figure 8b). During an 8-hour discharge, the thermal resistance follows the trend expected for radial conduction. For a 4-hour discharge, the resistance deviates from this expected trend around 60% state of charge. After this point, the resistance stays relatively constant until a region of the device becomes fully melted. This plateau suggests that natural convection starts to play an important role in heat transfer through the liquid layer.[7,18] Convection is more dominant at higher C-rates because the warmer channel wall results in a greater degree of buoyancy-induced circulation.

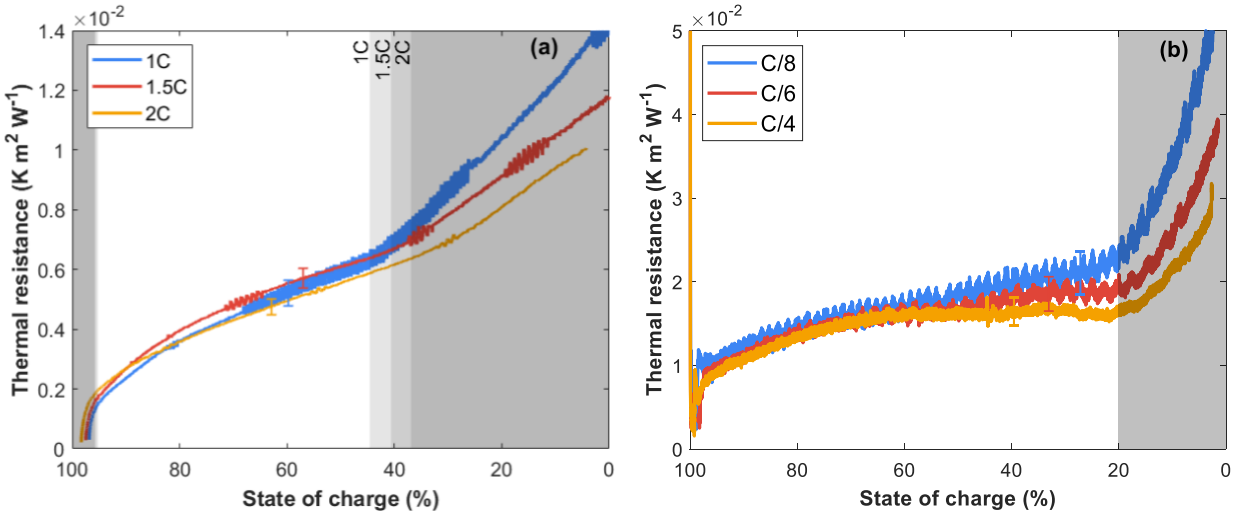

Figure 8: The total area-specific thermal resistances at three different discharge rates in the (a) microchannel PCM composite TES and (b) the ice-based TES. The greyed-out portions denote regions where the composite PCM has not started transitioning phase near the channel wall (left side), or when regions of the device fully melt resulting in a loss of heat transfer area (right side). The grey regions were identified with surface thermocouples in the microchannel composite TES and were approximated for the ice-based TES (see supplemental section S1). The error bars show representative experimental uncertainty for each run.

The surface resistances can also be extracted from the total thermal resistances shown in Figure 8. In the composite PCM device, a linear fit was performed for the measurements between the grey regions, and the surface resistance was found by evaluating the fit at the state of charge where liquid started to appear in the

device. The surface resistances are nearly constant for different heat transfer rates (between 2.15×10^{-3} and 2.35×10^{-3} K m^{-2} W^{-1}). This is anticipated because the surface resistance is not expected to change significantly with heat transfer rate since the flow is laminar and fully developed after ~10% of the channel length and the applied pressure is held constant (27.6 kPa).

The surface resistances in the ice-based TES device were also estimated using the same technique. Since the PCM melts radially away from the tube, the thermal resistance was fit to the natural-log-based function shown in Equation 10 (see section S3 in the supplemental information for more details).

$$R'' = A * \ln\left(\frac{\sqrt{\left(\frac{4}{\pi}S_t^2 - D_t^2\right)(1 - SOC) + D_t^2}}{D_t}\right) + B \tag{10}$$

This equation requires knowledge of the tube spacing (S_t) and outer diameter (D_t). The fit included data between 95% state of charge (after the initial transient that occurred while starting the system) and 65% state of charge. The minimum state of charge was limited to avoid regions where natural convection may play a larger role. The fit was evaluated at 100% state of charge to find the surface resistance since the ice is expected to be near the saturated solid state when fully charged. The surface resistance for the C/4 and C/6 cases were similar, at $(7.12\pm1.57)\times10^{-3}$ and $(7.55\pm2.19)\times10^{-3}$ K m^{-2} W^{-1}, respectively. The C/8 surface resistance was slightly higher, at $(8.75\pm3.36)\times10^{-3}$ K m^{-2} W^{-1}, which may be the result of experimental uncertainty or higher fluid convective resistances associated with lower flow rates.

Understanding how the surface resistances relate to the total can inform future design iterations aimed at boosting device performance. For example, the surface resistance of the ice-based TES device is nearly half of the total resistance before regions of the tank fully melt (~20% state of charge). This is a consequence of the relatively low glycol heat transfer coefficients and the plastic tubing used in the glycol coil. Although the system works well at low C-rates, the surface resistance would likely need to be reduced to discharge the tank over a shorter period.

The relative contributions of surface resistance in the PCM composite TES device are lower but depend on the applied pressure, as shown in Figure 9. The surface resistance decreases by nearly 60% when the pressure increases from 1 to 4 psi, but stays relatively constant with further increases in pressure. This trend is related to the contact resistance between the PCM composite and the fluid channel. The contact resistance is expected to decrease with higher applied pressures, but with diminishing returns.[21,22]

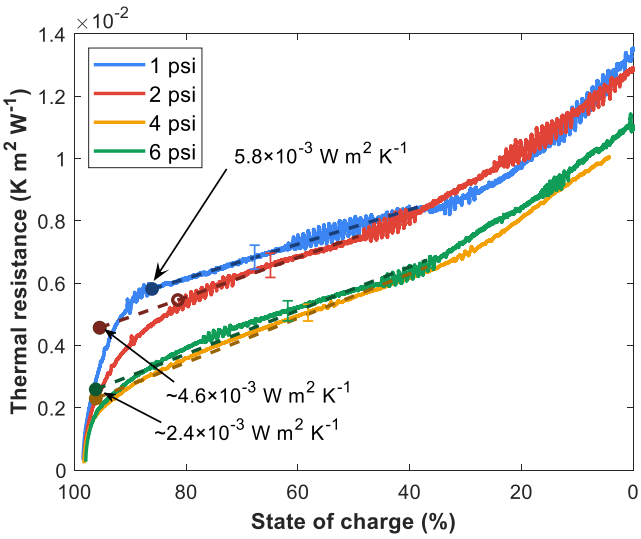

Figure 9: The total area-specific thermal resistance and extrapolated surface resistances as a function of applied pressure when the microchannel PCM composite heat exchanger is discharged at 1.5C. The error bars show representative experimental uncertainty for each run. The grey shaded regions were removed for clarity, but the dashed linear fit lines show the valid region for each pressure. The circles show the state of charge where liquid starts to form (supplemental section S1) and the associated surface resistance. The surface thermocouples did not show a distinct change in slope to indicate the presence of liquid for the experiment performed at 2 psi. The start and end of the gradual change in slope are shown as the dark red filled and unfilled points, respectively.

Theoretically, the total thermal resistances shown in Figure 9 should follow the same trend but be shifted up or down based on the applied pressure. However, these results show some unexpected differences in the shapes of these curves, which may indicate power degradation of the device with repeated use. To further investigate these trends, we compared the resistances at 4 psi as a function of the cycle number (Figure 10). The total resistance increases as the device is cycled, which is also likely linked to the loss of PCM from the graphite. The leaked PCM that settles near insulated surfaces of the composite cannot accept heat as readily because of its low thermal conductivity. This lowers the effective capacity at high power rates and will cause the resistances to increase faster over the course of the experiment. Additionally, any PCM that settles between the composite and the fluid channel will increase the surface resistance and hinder heat transfer into the material. Finally, non-uniform distribution of the PCM in the graphite could occur after cycling, which could theoretically change the shape of the resistance profile. Together these effects are likely contributing to the trends shown in Figure 10. To minimize the impact of degradation in the results shown in Figures 8 and 9, we only compared data taken sequentially. The data for 4, 6, 2 and 1 psi shown in Figure 9 correspond to cycles 10, 12, 13 and 15 in Figure 10, respectively. The order that data was taken explains some of the unexpected trends in Figure 9, including that the measured thermal resistance for 6 psi was higher than for 4 psi.

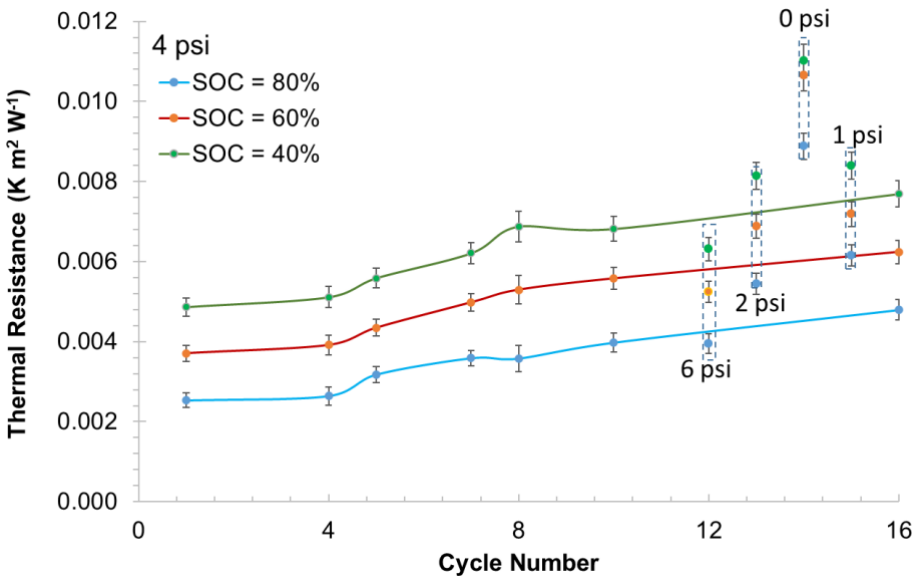

Figure 10: The measured area-specific thermal resistance at 80%, 60%, and 40% state of charge for the microchannel PCM composite heat exchanger when discharged with 4 psi of pressure applied and at powers between 1C and 2C. The results at different applied pressure are shown for reference (more details in Figure 9). Under ideal conditions with no degradation, the resistance for all 4 psi cases should be similar. The measurements indicate a systematic increase in resistance with cycles, which might be related to leakage of phase changing material out of the graphite matrix or the reduction in its thermal conductivity on cycling.

Previous work has shown the material used in this study (expanded graphite composite PCMs) can experience degradation in thermal conductivity and latent heat when cycled.[23] Decreases in latent heat are usually due to PCM loss from the graphite material. Expanded graphite-based PCM composites can lose up to 50% of their mass over repeated cycles,[24] although the magnitude of the loss will depend on the geometry of the composite and the characteristics of the expanded graphite. In this work, the composite was encapsulated and did not lose capacity while cycled, but PCM loss from the graphite along with any reduction in thermal conductivity still led to an increase in resistances over time. This degradation must be overcome before tetradecane/graphite composites can be used in actual TES systems.[25]

Conclusion

This paper presents experimental methods to measure the total capacity and thermal resistance in fluid-coupled TES devices. These two parameters drive device performance because capacity dictates the maximum attainable energy density, and the internal resistances drive how much thermal energy can be extracted before the outlet temperature reaches its cutoff (actual energy density). We also describe a method to determine the breakdown of resistances in the device to help identify any thermal bottlenecks. Together, these measurements can help drive future design iterations toward both high energy and power densities.

Additionally, these methods can be used to characterize degradation in PCM TES devices. The capacity experiment can be run at regular intervals during cycling to quantify irreversible loss in storage capacity that could result from a decrease in latent heat or from PCM leaking out of the device. The resistance measurement can also detect evidence of degradation, as we demonstrated using an expanded graphite-tetradecane composite PCM. Faster increases in resistances between successive cycles could be related to capacity loss but could also result from increases in the PCM or surface resistances. These experiments together can help identify the cause of energy density loss over the life of a TES system, which will help designers develop robust devices that can be effectively integrated into thermal equipment.

These methods provide some new tools to characterize TES heat exchangers, but more work is needed to fully understand how they will operate in different scenarios. Future work should focus on developing additional device-level characterization techniques to determine properties like drive cycle performance and lifetime. A full suite of characterization tools would allow designers to develop robust, high-capacity thermal energy storage devices for a range of applications.

Acknowledgements

This work was authored by the National Renewable Energy Laboratory, operated by Alliance for Sustainable Energy, LLC, for the U.S. Department of Energy (DOE) under Contract No. DE-AC36-08GO28308. Funding provided by the U.S. Department of Energy Building Technologies Office. The views expressed in the article do not necessarily represent the views of the DOE or the U.S. Government. The U.S. Government retains and the publisher, by accepting the article for publication, acknowledges that the U.S. Government retains a nonexclusive, paid-up, irrevocable, worldwide license to publish or reproduce the published form of this work, or allow others to do so, for U.S. Government purposes.

The authors would like to thank Erin Lewis and Greg Shoukas from NREL for their help setting up the experiments, and Anurag Goyal from the Indian Institute of Technology Delhi for initial discussions regarding TES measurement techniques.

References

1 Barako, M. T. *et al.* Optimizing the design of composite phase change materials for high thermal power density. *Journal of Applied Physics* **124**, 145103, doi:10.1063/1.5031914 (2018).

2 Yang, T. *et al.* A composite phase change material thermal buffer based on porous metal foam and low-melting-temperature metal alloy. *Applied Physics Letters* **116**, 071901, doi:10.1063/1.5135568 (2020).

3 Cabeza, L. F., Castell, A., Barreneche, C., de Gracia, A. & Fernández, A. I. Materials used as PCM in thermal energy storage in buildings: A review. *Renewable and Sustainable Energy Reviews* **15**, 1675-1695, doi:10.1016/j.rser.2010.11.018 (2011).

4 Mavrigiannaki, A. & Ampatzi, E. Latent heat storage in building elements: A systematic review on properties and contextual performance factors. *Renewable and Sustainable Energy Reviews* **60**, 852-866, doi:10.1016/j.rser.2016.01.115 (2016).

5 Xiao, Q., Fan, J., Li, L., Xu, T. & Yuan, W. Solar thermal energy storage based on sodium acetate trihydrate phase change hydrogels with excellent light-to-thermal conversion performance. *Energy* **165**, 1240-1247, doi:10.1016/j.energy.2018.10.105 (2018).

6 Laughlin, R. B. Pumped thermal grid storage with heat exchange. *Journal of Renewable and Sustainable Energy* **9**, 044103, doi:10.1063/1.4994054 (2017).

7 Zhou, D., Zhao, C. Y. & Tian, Y. Review on thermal energy storage with phase change materials (PCMs) in building applications. *Applied Energy* **92**, 593-605, doi:10.1016/j.apenergy.2011.08.025 (2012).

8 Mohamed, S. A. *et al.* A review on current status and challenges of inorganic phase change materials for thermal energy storage systems. *Renewable and Sustainable Energy Reviews* **70**, 1072-1089, doi:10.1016/j.rser.2016.12.012 (2017).

9 Sharma, A., Tyagi, V. V., Chen, C. R. & Buddhi, D. Review on thermal energy storage with phase change materials and applications. *Renewable and Sustainable Energy Reviews* **13**, 318-345, doi:10.1016/j.rser.2007.10.005 (2009).

10 Kenisarin, M. M. High-temperature phase change materials for thermal energy storage. *Renewable and Sustainable Energy Reviews* **14**, 955-970, doi:10.1016/j.rser.2009.11.011 (2010).

11 Pielichowska, K. & Pielichowski, K. Phase change materials for thermal energy storage. *Progress in Materials Science* **65**, 67-123, doi:10.1016/j.pmatsci.2014.03.005 (2014).

12 Stroe, D.-I., Swierczynski, M., Stroe, A.-I. & Knudsen Kær, S. Generalized Characterization Methodology for Performance Modelling of Lithium-Ion Batteries. *Batteries* **2**, doi:10.3390/batteries2040037 (2016).
13 Woods, J. *et al.* Rate capability and Ragone plots for phase change thermal energy storage. *Nature Energy* **6**, 295-302, doi:10.1038/s41560-021-00778-w (2021).
14 Sung, P., Savvides, A. & Srivastava, M. B. in *ISLPED'01: Proceedings of the 2001 International Symposium on Low Power Electronics and Design (IEEE Cat. No.01TH8581).* 382-387.
15 Barai, A., Uddin, K., Widanage, W. D., McGordon, A. & Jennings, P. A study of the influence of measurement timescale on internal resistance characterisation methodologies for lithium-ion cells. *Scientific Reports* **8**, 21, doi:10.1038/s41598-017-18424-5 (2018).
16 Waag, W., Käbitz, S. & Sauer, D. U. Experimental investigation of the lithium-ion battery impedance characteristic at various conditions and aging states and its influence on the application. *Applied Energy* **102**, 885-897, doi:10.1016/j.apenergy.2012.09.030 (2013).
17 Reddy, T. B. & Linden, D. *Linden's Handbook of Batteries, Fourth Edition*. 4th ed. edn, 3.1-3.22 (McGraw-Hill Education, 2011).
18 Garcia, P., Olcese, M. & Rougé, S. Experimental and Numerical Investigation of a Pilot Scale Latent Heat Thermal Energy Storage for CSP Power Plant. *Energy Procedia* **69**, 842-849, doi:10.1016/j.egypro.2015.03.102 (2015).
19 Zhu, Y. & Zhang, Y. Modeling of thermal processes for internal melt ice-on-coil tank including ice-water density difference. *Energy and Buildings* **33**, 363-370, doi:https://doi.org/10.1016/S0378-7788(00)00118-3 (2001).
20 Kibria, M. A., Anisur, M. R., Mahfuz, M. H., Saidur, R. & Metselaar, I. H. S. C. Numerical and experimental investigation of heat transfer in a shell and tube thermal energy storage system. *International Communications in Heat and Mass Transfer* **53**, 71-78, doi:https://doi.org/10.1016/j.icheatmasstransfer.2014.02.023 (2014).
21 Yovanovich, M. in *16th Thermophysics Conference Fluid Dynamics and Co-located Conferences* (American Institute of Aeronautics and Astronautics, 1981).
22 Mikić, B. B. Thermal contact conductance; theoretical considerations. *International Journal of Heat and Mass Transfer* **17**, 205-214, doi:https://doi.org/10.1016/0017-9310(74)90082-9 (1974).
23 Wang, Q., Zhou, D., Chen, Y., Eames, P. & Wu, Z. Characterization and effects of thermal cycling on the properties of paraffin/expanded graphite composites. *Renewable Energy* **147**, 1131-1138, doi:10.1016/j.renene.2019.09.091 (2020).
24 Zhao, Y. *et al.* Expanded graphite – Paraffin composite phase change materials: Effect of particle size on the composite structure and properties. *Applied Thermal Engineering* **171**, doi:10.1016/j.applthermaleng.2020.115015 (2020).
25 Fauzi, H., Metselaar, H. S. C., Mahlia, T. M. I., Silakhori, M. & Ong, H. C. Thermal characteristic reliability of fatty acid binary mixtures as phase change materials (PCMs) for thermal energy storage applications. *Applied Thermal Engineering* **80**, 127-131, doi:10.1016/j.applthermaleng.2015.01.047 (2015).